July, 2003

Vibration of Flex Circuits in Hard Disk Drives

Jonathan A. Wickert, *Carnegie Mellon University*

Vibration of Flex Circuits in Hard Disk Drives

J. A. Wickert
Fellow ASME,
Department of Mechanical Engineering,
Carnegie Mellon University,
Pittsburgh, PA 15213

A flex circuit connects the stationary electronic components in a hard disk drive to the rotating arm that carries the read/write heads and positions them above data tracks on the disk. Flex circuits are conventionally formed as a laminate of polyimide substrate, adhesive, and copper conductors. Deformation of a flex circuit is discussed in the context of the following stages: the initial unstressed shape, configurations in which stresses set and relax in response to elevated temperature, equilibrium, and small amplitude vibration. The model involves displacements of the flex circuit in the directions tangent and normal to the local equilibrium shape, and those motions couple with the arm's dynamics. Nonlinearity associated with finite curvature, partial elastic springback, and the arm's geometry and inertia properties are incorporated within the vibration model to predict system-level natural frequencies, mode shapes, and coupling factors between the circuit and the arm. Laboratory measurements using noncontact laser interferometry validate the model with respect to the circuit's shape, stiffness, restoring moment, and natural frequencies. The primary degrees of freedom for optimizing flex circuit design are the thicknesses of the individual layers within the circuit, free length, and the locations and slopes of the circuit's attachment points to the arm and electronics block. The model's predictions and trends developed from a case study in free length are discussed with a view toward reducing coupling between the circuit and arm in certain vibration modes.
[DOI: 10.1115/1.1547661]

1 Introduction

The storage density of hard disk drives, as measured by the number of data bits captured within a unit area, has grown at a historical rate of about 60% per year, and that rate has accelerated recently to more than 100% per year. In a similar vein, the cost associated with storing a megabyte of data has fallen by over four orders of magnitude during the past two decades. With the physical limit for the density of magnetic disk recording now appearing on the horizon, higher-precision requirements are being placed on the vibration of each structural and actuation component.

By way of background and motivation, the construction of a hard disk drive is shown in the photograph of Fig. 1. Data is stored as magnetic transitions on the thin media layer that coats the glass disks. The arm pivots about a fixed bearing, and it is driven by a voice coil that swings between two permanent magnets. The read/write heads are located at the tip of the arm above each disk surface, but they are not discernible in Fig. 1 because of their small size. The particular drive shown in the figure has a total of ten read/write heads.

The voice coil and its companion servo system slew the heads to a desired cylinder of data, and follow it in the presence of disk runout, vibration, windage, and other disturbances. Electrical leads are routed to each read/write head to carry the recording and readback signals, and other larger leads power the voice coil. Each head and coil wire is integrated within a flat and flexible circuit that conveys all of the electrical signals between the (rotating) arm and the (stationary) electronics on the drive's body. This overall construction is shown schematically in Fig. 2. In a typical embodiment, the flex circuit is a polyimide film laminate having rolled annealed copper wires in its conductor layer. Flex circuits replace conventional multi-lead wiring and combine electrical functionality with mechanical flexibility, which in turn can potentially introduce unwanted vibration. Quite aside from hard disk drives, other types of flex circuits are used in avionics packages, gyroscopes, hearing aids, and cardiac pacemakers.

Contributed by the Technical Committee on Vibration and Sound for publication in the JOURNAL OF VIBRATION AND ACOUSTICS. Manuscript received May 2002; revised October 2002. Associate Editor: Chin An Tan.

The mechanical behavior and vibration of a hard drive's disks, motor, spindle, bearings, voice coil, and other elements have been the subject of substantial engineering development effort since the first introduction of a hard disk drive in 1956. As drives have become more sophisticated, sources of vibration that had previously been within tolerance limits have become the focus of further improvement efforts. In particular, the vibration of flex circuits and their coupling with motion of the read/write heads are now factors in high density recording applications. No longer viewed as a lightweight appendix to the arm and voice coil, the flex circuit has dynamics that couple through the arm and produce track positioning errors.

Reducing flex circuit vibration in certain modes is a potential strategy for improving transient settling response after a seek operation to a new data track. From the modeling perspective, an objective of this investigation is to better understand the flex circuit's equilibrium shape involving finite deformation and partial elastic springback, and the character of its small amplitude vibration about equilibrium. Of particular interest are the flex circuit's static shape at a specified arm rotation angle, natural frequencies, and coupling to the arm and read/write heads in each mode. In what follows, the roles played by such parameters as the circuit's laminated structure, finite curvature, free length, and boundary conditions at the arm and electronics block are explored.

2 Material Characteristics and Loading Sequence

In Fig. 3, the two micrographs of a flex circuit's cross-section describe the internal morphology and dimensions of the several material layers. In optical diagnostics, a segment of the flex circuit was embedded in epoxy, diced, and polished smooth. A thin layer of gold was then sputtered onto the surface of the cross-section to enhance imaging. The particular circuit of Fig. 3 is formed as a symmetric sandwich laminate of two $h_p = 31\ \mu$m thick polyimide layers on either side of flat copper electrical leads. Kapton® is often used as the substrate material, and it is chosen on the basis of electrical, mechanical, and thermal properties. In Fig. 3(*a*), a matrix of epoxy bonds the polyimide layers to the conductors, and the thickness of the intervening adhesive is $h_a = 13\ \mu$m. The circuit comprises twenty conductors having common $h_c = 26\ \mu$m

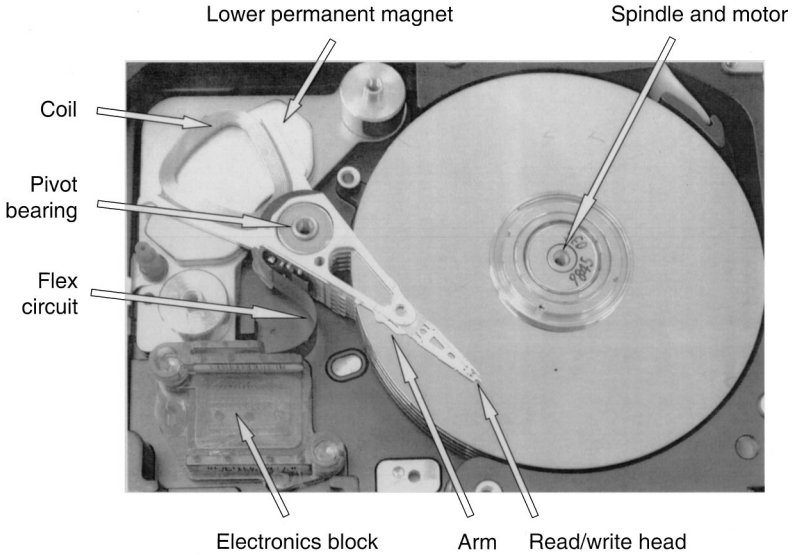

Fig. 1 Photograph depicting certain mechanical components within a hard disk drive used for computer data storage

thickness, and one of four different widths depending on the type of electrical signal being carried. Some $\delta = 67\%$ of the flex circuit's $b = 11.15$ mm width is associated with the conductors, and the remaining fraction of space between the conductors remains insulated by adhesive. Figure 3(*b*) depicts a second portion of the same flex circuit, and its image is spaced width-wise relative to Fig. 3(*a*). Three adjacent conductors, slight variation in the adhesive thickness, and indentation of the conductor into the lower substrate are visible features. The cumulative thickness is $h = h_c + 2(h_p + h_a) = 114\ \mu$m, and the flex circuit has linear density 2.38 g/m in the direction along its free length L.

Vibration of the flex circuit depends in part on its equilibrium curvature and internal loads, which are distinguished from their counterparts in the circuit's natural state where no reactions are applied through attachment to the arm and electronics block. Further, the flex circuit's stresses, particularly in the adhesive layer, are known to partially relax with time and temperature. Deformation from the initial free shape, through finite motion to equilibrium, and ultimately to small amplitude vibration are broken down in the following sequence of loading states:

Initial $\mathbf{S}^{(0)}$ The flex circuit is specified to be initially unstressed and straight. Imperfections that are present as a result of the circuit's production or the drive's final assembly could be incorporated at this stage by specifying a functional form of curvature $k^{(0)}(s)$, where $s \in (0,L)$ denotes arc length, but such effects are not considered at this first level of approximation.

Set $\mathbf{S}^{(1)}$ Referring to Fig. 2, the flex circuit is bent from $S^{(0)}$ and attached to the arm and electronics block. Elements within it are subjected to tension $T(s)$, shear force $N(s)$, and bending moment $M(s)$. During the process to $S^{(1)}$, the circuit undergoes finite

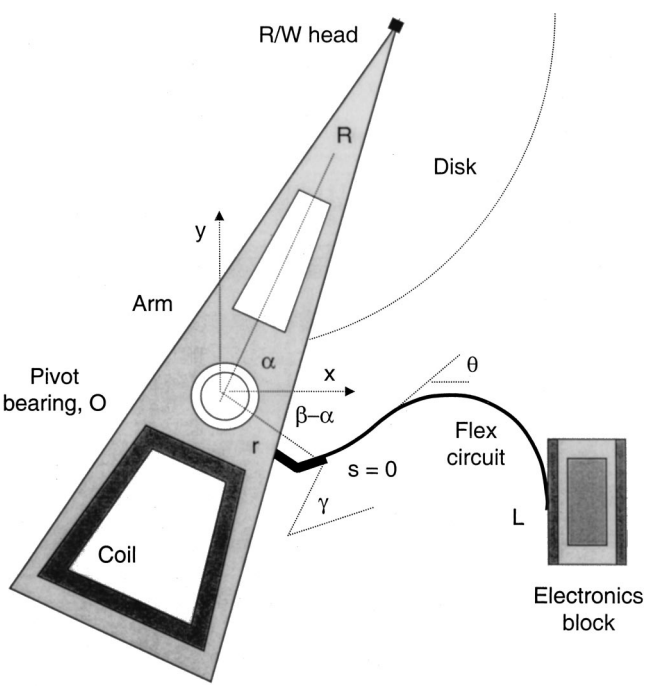

Fig. 2 Schematic of the equilibrium and vibration model for the arm and flex circuit mechanism

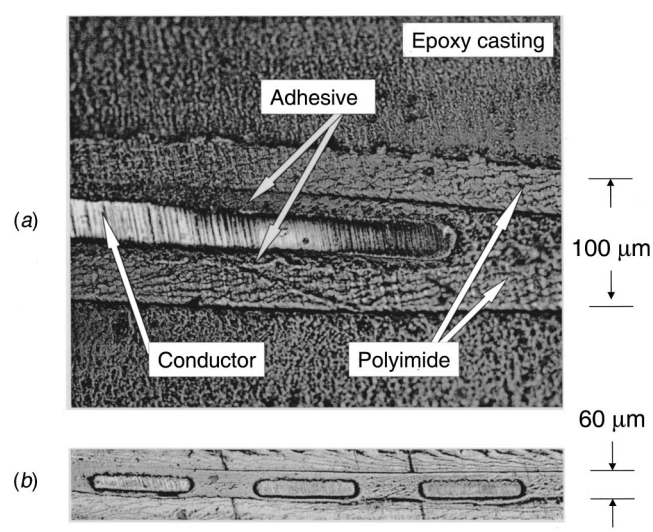

Fig. 3 (*a*) Brightfield and (*b*) differential interference contrast micrographs of flex circuit cross-sections. The images depict the construction morphology and the thicknesses of the polyimide, conductor, and adhesive layers.

deformation to the new shape of curvature $k^{(1)}$. The coordinates (x_L, y_L) of the contact point and the angle θ_L of approach at the electronics block are specified. Rotation α of the arm is an independent variable in $S^{(1)}$, and together with the geometric parameters β, γ, and r defined in Fig. 2, its value sets the circuit's conditions

$$x(0)=r\cos(\alpha-\beta) \quad y(0)=r\sin(\alpha-\beta) \tag{1}$$

$$\theta(0)=\alpha-\gamma \tag{2}$$

at its endpoint $s=L$. In $S^{(1)}$, the arm is held by an external agent at an angle that could correspond to the disk's inner (ID) or outer (OD) diameters, or the load-unload (LU) support where the arm is parked when the drive is not in use.

Springback $S^{(2)}$ During both its production and day-to-day usage, the flex circuit is exposed to elevated temperature. Certain fabrication stages take place at 80°C; an assembly-level wash/dry cycle occurs at 85°C; and the internal environment of a performance drive can reach 50–60°C. By comparison, the glass transition temperature of an adhesive commonly used within flex circuits lies in the range 50–95°C. In the springback stage, while the flex circuit remains attached to the arm and electronics block in $S^{(1)}$, stresses are allowed to partially relax and the circuit assumes the new natural state $S^{(2)}$. To characterize this process, thermal cycling experiments were conducted with the arm locked at the disk's inner diameter ($\alpha_{\mathrm{ID}}=64$ deg) and the assembly held at 45°C for one hour. After having cooled to ambient temperature, the arm and flex circuit assumed nearly that point as the new equilibrium configuration. The arm was then pivoted to the disk's outer diameter ($\alpha_{\mathrm{OD}}=32$ deg), thermally cycled, and observed to assume a nearby position in equilibrium. During those processes, however, the stresses within the flex circuit were only partially reduced. Indeed, when the circuit was cut free and released, it assumed a new natural state having shape and curvature somewhat between $k^{(0)}$ and $k^{(1)}$. The empirical factor p is introduced to quantify the amount of elastic springback that occurs when the flex circuit is unloaded, and the curvature in $S^{(2)}$ is defined $k^{(2)}=(1-p)k^{(1)}$. When $p=1$, the circuit behaves elastically, is unaffected by exposure to elevated temperature, and returns to its initial straight shape when unloaded from $S^{(1)}$. On the other hand, when $p=0$, the flex circuit assumes $S^{(1)}$ as the new natural state. In practice, the actual loading process and $k^{(2)}$ lie between these two extremes, and they change in a time-, temperature-, and history-dependent manner as the arm continuously slews between the disk's ID and OD. In the baseline parameters of Table 1, the value $p=0.55$ was determined by experience in thermally cycling several disk drives and examining the circuits when they were cut and released from the arm and electronics block. The flex circuits were photographed, and their natural shapes were compared to those predicted by the equilibrium model described below at various levels of springback. Parameter p was then adjusted by cut-and-try until the predicted and measured natural shapes were agreeably close.

Equilibrium $S^{(3)}$ From the natural configuration $S^{(2)}$, the flex circuit is imagined to be re-attached to the arm and electronics block. With no external torque M_o about the pivot point being applied by the voice coil, the arm rotates to equilibrium in response to the combined influence of the tension, shear force, and bending moment at $s=0$. At this stage, the arm's equilibrium angle and the circuit's curvature are denoted by α_* and $k_*=k^{(3)}$, respectively.

Deformed $S^{(4)}$ In this loading stage, the flex circuit is elastically deformed about equilibrium, corresponding to static slew at a certain angle, to small amplitude vibration of the flex circuit about equilibrium, or to finite amplitude vibration. The tension, shear force, and bending moment are each incremented relative to their equilibrium values. Motion of the flex circuit is resolved into the directions tangent and normal to the local equilibrium, and those displacements are denoted by $u(s,t)$ and $v(s,t)$, respectively.

Table 1 Baseline parameters for the arm and flex circuit's equilibrium and vibration models

Flex Circuit	
Width, b	11.1 mm
Thickness	
Polyimide layer, h_p	31 μm
Adhesive layer, h_a	13 μm
Conductor layer, h_c	26 μm
Cumulative, h	114 μm
Conductor fraction, δ	67%
Free length, L	31 mm
Composite linear density, ρA	2.38 g/m
Modulus	
Polyimide, E_p	2.75 GPa
Adhesive, E_a	1.03 GPa
Conductor, E_c	115 GPa
Springback ratio, p	0.55
Composite bending stiffness, EI	$4.78\times(10^{-6})$ N·m^2
Composite axial stiffness, EA	$2.45\times(10^4)$ N
Arm	
Attachment radius, r	10.6 mm
Read/write head radius, R	43.8 mm
Attachment angle, β	95°
Offset angle, γ	8°
Angles	
Load-unload, α_{LU}	23°
Disk OD, α_{OD}	32°
Disk ID, α_{ID}	64°
Inertia, m	17.2 g
Radius of gyration, κ	11.9 mm
Electronics Block	
Coordinates, (x_L, y_L)	(24, −11) mm
Tangency angle, θ_L	−90°

3 Equilibrium Shape, Loads, and Stresses

The flex circuit's shape in $S^{(3)}$ is defined parametrically by the coordinates $(x(s),y(s))$. With the nomenclature $(\bullet)'=d/ds$, equilibrium in the local tangential and normal directions is governed by the force and moment balances [1]

$$T'=Nk, \quad N'=-Tk, \quad k'=-N/EI+k^{(2)'} \tag{3}$$

in which the constitutive relation $M=EI(k-k^{(2)})$ has been embedded. The circuit's bending stiffness is given by

$$EI=\frac{1}{12}E_c h_c^3\delta b+\frac{1}{12}E_a h_c^3(1-\delta)b+2E_a\left(\frac{1}{12}bh_a^3+\frac{1}{4}bh_a(h_c+h_a)^2\right)+2E_p\left(\frac{1}{12}bh_p^3+\frac{1}{4}bh_p(h_c+h_p+2h_a)^2\right) \tag{4}$$

where values for the elastic constants of the conductor E_c, polyimide E_p, and adhesive E_a are listed in Table 1. While Eq. (4) is specific to the cross-sectional construction of Fig. 3, the treatment can be adapted for other geometries.

On the basis of measured layer thicknesses and published elastic constants [2] in Table 1, the circuit's composite bending stiffness is $EI=4.78\times10^{-6}$ N·m^2. The conductor layer contributes 26% to the stiffness, the polyimide layer 71%, and the adhesive layer only 3%. This value of EI was validated by both static bending and natural frequency measurements conducted with a circuit segment that was embedded as a cantilever in an epoxy casting. In the static test, the segment was mounted on a micrometer translation stage, and under specified displacement, the force applied to it's tip was measured. The signal from a planar beam sensor (Futek FR-1020) was conditioned and amplified to provide a calibrated and linear force response for loads up to 295 mN. The

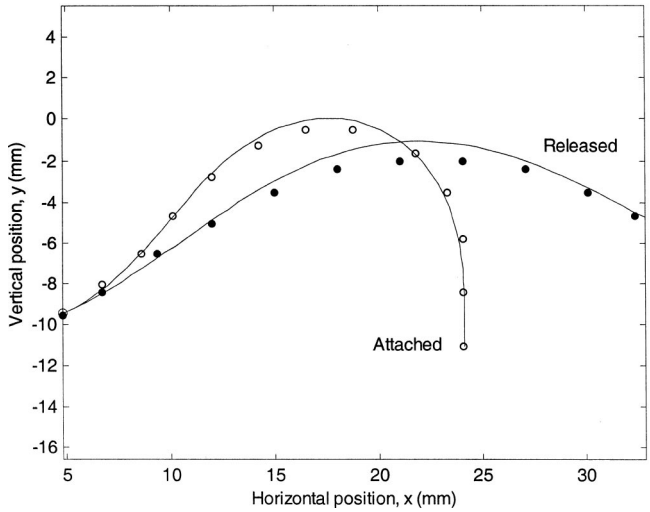

Fig. 4 Predicted (——) and measured shapes of the flex circuit in equilibrium with attachment to the arm and electronics block, and in its natural state. The shapes extracted from photographs of the circuit in the two states are denoted by the (○) and (●) data points, respectively.

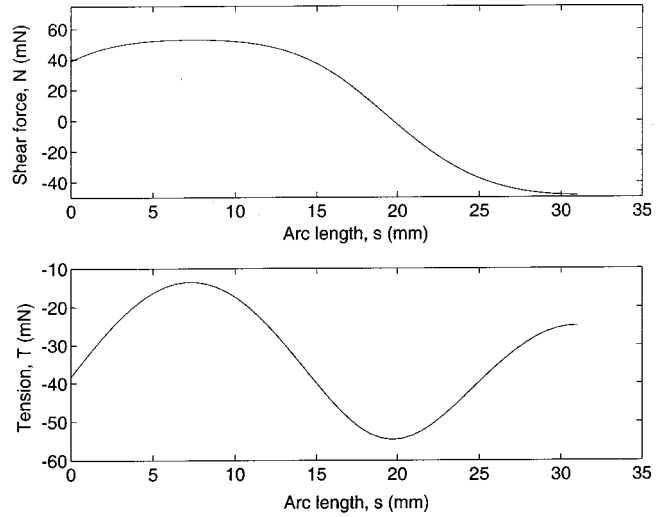

Fig. 5 Equilibrium tension and shear force along the circuit's arc length

stiffness recorded on this basis was 4.60×10^{-6} N·m^2. In the second validation test, the value 4.91×10^{-6} N·m^2 was determined by measuring the segment's two lowest natural frequencies and matching them to the values expected for a cantilever. In the calculations described below, the stiffness value determined from Eq. (4) was used.

The circuit's equilibrium curvature is determined by integrating Eqs. (3), and its shape is found subsequently from the kinematic relations

$$x' = \cos\theta, \quad y' = \sin\theta, \quad \theta' = k(s) \tag{5}$$

subject to position and slope conditions at $s=0$ and L. While some rotation between the circuit and arm does occur locally at $s=0$, that effect is neglected in this first approximation, recognizing that the resulting model may overestimate the circuit's actual boundary stiffness.

Solutions to Eqs. (3) and (5) are found through a shooting method in which the boundary value problem in x, y, and θ is converted to an initial value problem, and then solved iteratively. Estimates for (initially unknown) $N(0)$, $T(0)$, and $k(0)$ are assigned, and the system of differential equations is integrated numerically. The values $x(L)$, $y(L)$, and $\theta(L)$ which result from that calculation do not, in general, satisfy the endpoint constraints. In iteration, $N(0)$, $T(0)$, and $k(0)$ are then adjusted through a nonlinear minimization scheme until each kinematic condition is satisfied within desired tolerance.

On the basis of the parameters in Table 1, Fig. 4 depicts simulated and measured shapes of the flex circuit in its natural ($S^{(2)}$) and equilibrium ($S^{(3)}$) states. The data points shown in the figure represent coordinate locations as extracted from photographs of the circuit in the two configurations. Curvature in the natural state was set with the arm held at the disk's OD and the springback constant being $p=0.55$. At the equilibrium angle $\alpha_*=26.4$ deg, the tension, shear force, and bending moment applied by the flex circuit to the arm produce no resultant torque about the pivot bearing. Their variations in response to first-order changes in α, however, are captured by stiffness 10.2 mN·mm/deg.

The equilibrium tension and shear force distributions along the circuit are shown in Fig. 5. The circuit is compressed over its entire length with the minimum, mean, and maximum loading values for T being -55, -33, and -14 mN, respectively. The zero crossing in shear occurs at a distance approximately 64% along the circuit's length from the arm. While the average strain over the cross-section is only $T/EA\approx-1.3\times10^{-6}$ with

$$EA = E_c h_c b\,\delta + 2E_a h_a b + E_a h_c b(1-\delta) + 2E_p h_p b \tag{6}$$

the peak bending strain $h_c|k_* - k^{(2)}|/2$ within the conductor layer is 0.12%. For other free lengths, arm positions, or endpoint locations, local yielding could occur within the ductile conductor.

As the arm slews about equilibrium, the flex circuit bends further to $S^{(4)}$ as shown in Fig. 6. The voice coil applies the static bias torque

$$M_o = T(0)r\sin(\beta-\gamma) + N(0)r\cos(\beta-\gamma) + M(0) \tag{7}$$

which increases in Fig. 7 from zero at equilibrium to the maximum value 0.35 N·mm at the disk's ID. Multiple measurements of the torque were made for one disk drive at four different slew angles, and those results are also shown in Fig. 7. The indicated variation of M_o is representative of such measurements and captures hysteresis in the circuit, and friction in the pivot bearing and

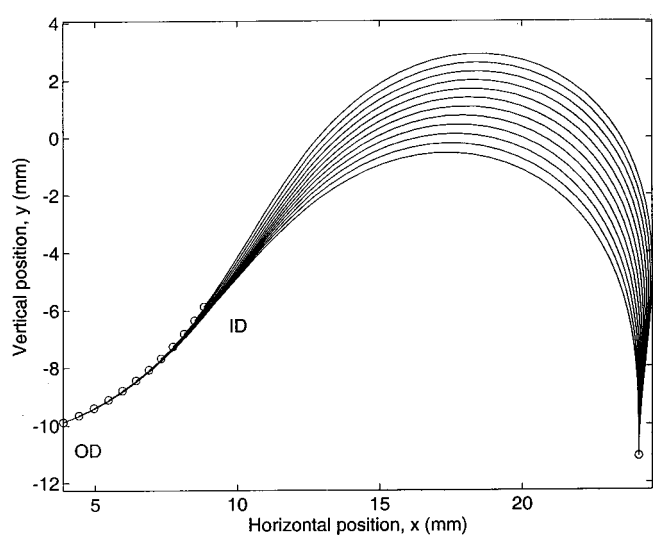

Fig. 6 Variation of the flex circuit's static shape for arm positions which range between the disk's outer and inner diameters. For each arm position, the locations of the circuit's endpoints are denoted by (○).

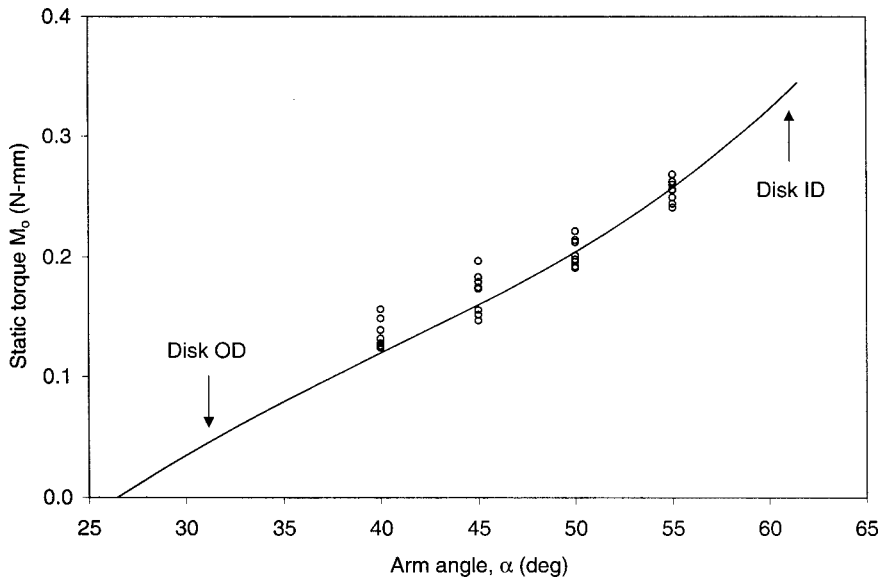

Fig. 7 Predicted (——) and measured (○) dependencies of the static restoring moment for arm positions between the disk's outer and inner diameters

supports. The trend in Fig. 7 is agreeably linear over the operating range, although the circuit's stiffness $dM_o/d\alpha$ does decrease in the disk's mid-diameter range, and grow again for slew angles near the ID.

Figure 8 depicts the manner in which the flex circuit's equilibrium shape changes as a function of its free length. Results are shown for simulations in which L varies between 70% and 130% of its nominal value. With the other parameters of Table 1 remaining fixed, the corresponding changes to the arm's equilibrium angle and the circuit's static stiffness are listed in Table 2.

4 Natural Frequencies, Vibration Modes, and Coupling

For small amplitude vibration in $S^{(4)}$, the shear, tension, and curvature are expanded

$$N = N_* + \epsilon N_1 + \cdots \tag{8}$$

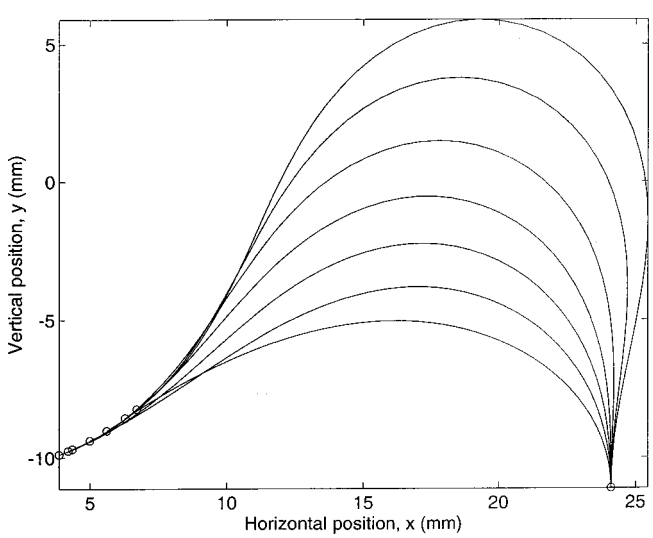

Fig. 8 Flex circuit equilibrium shapes predicted for free length's which range between 70% and 130% of the nominal value in Table 1

$$T = T_* + \epsilon T_1 + \cdots \tag{9}$$

$$k = k_* + \epsilon k_1 + \cdots \tag{10}$$

about their equilibrium values, denoted by $(\bullet)_*$. Here $\epsilon \ll 1$ is a dimensionless scaling parameter used in the linearization, and the first-order corrections are written [3,4]

$$N_1 = -EI(v_{,ss} + (k_* u)_{,s})_{,s} \tag{11}$$

$$T_1 = EA(u_{,s} - k_* v) \tag{12}$$

$$k_1 = (v_{,s} + (k_* u))_{,s} \tag{13}$$

in terms of the circuit's tangential and normal displacements. Here the comma-subscript notation signifies partial differentiation. The equations of motion become

$$\rho A u_{,tt} - T_{1,s} + N_* k_1 + k_* N_1 = 0 \tag{14}$$

$$\rho A v_{,tt} - N_{1,s} - T_* k_1 - k_* T_1 = 0 \tag{15}$$

where ρA is the circuit's mass-per-unit-length.

Vibration of the flex circuit and arm couple through

$$m\kappa^2 \ddot{\alpha}_1 = T_1(0,t) r \sin(\beta - \gamma) + N_1(0,t) r \cos(\beta - \gamma) + M_1(0,t) \tag{16}$$

where m is the arm's mass, κ is it's radius of gyration about the pivot bearing, and α_1 is the first-order rotation about α_*. The time-dependent incremental loads in Eq. (16) are evaluated at the circuit's connection point to the arm. Although not considered here, the effects of the voice coil's driving torque and damping in

Table 2 Dependence of the equilibrium angle and the circuit's stiffness with respect to free length over a range 70% to 130% of nominal

Length ratio	Length (mm)	Equilibrium angle (deg)	Stiffness (mN·mm/deg)
70%	21.7	41.3	63.6
80%	24.8	33.0	40.0
90%	27.9	28.4	20.2
100%	31.0	26.4	10.2
110%	34.1	29.3	5.6
120%	37.2	36.9	5.0
130%	40.3	44.2	5.8

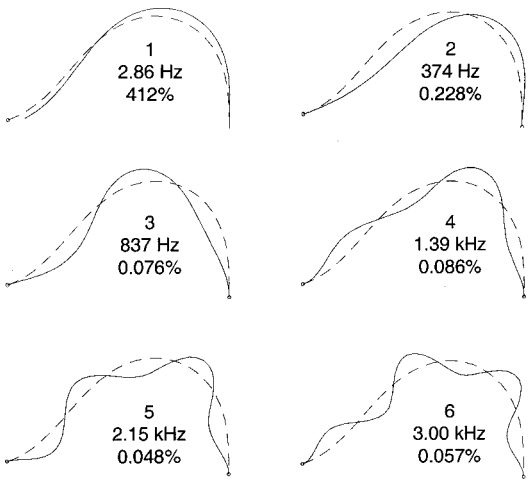

Fig. 9 First six vibration modes (——) shown superposed on the equilibrium shape (— — —). Each element of the figure is annotated with the predicted natural frequency and displacement ratio η.

the pivot bearing could be incorporated in Eq. (16) at this stage for direct numerical simulation or control system studies. Motion of the circuit and arm are also constrained through

$$u(0)=r\sin(\beta+\gamma)\alpha_1 \tag{17}$$

$$v(0)=r\cos(\beta+\gamma)\alpha_1, \tag{18}$$

and the conditions $u=0$, $v=0$, and $v_{,s}+k_* u=0$ at $s=L$.

The flex circuit is substantially stiffer for displacements in u than v, and the ratio of longitudinal to flexural stiffness is measured by the dimensionless parameter $(EAL^2)/(EI)$, which is $O(10^6)$ for the problem at hand. On the time scales of the lower transverse modes, tension variations propagate almost instantaneously, and the explicit appearance of u in the equations of motion can be suppressed by approximating T_1 as a function of time alone. After integrating Eq. (12) in this manner, the longitudinal displacement field is approximately [5]

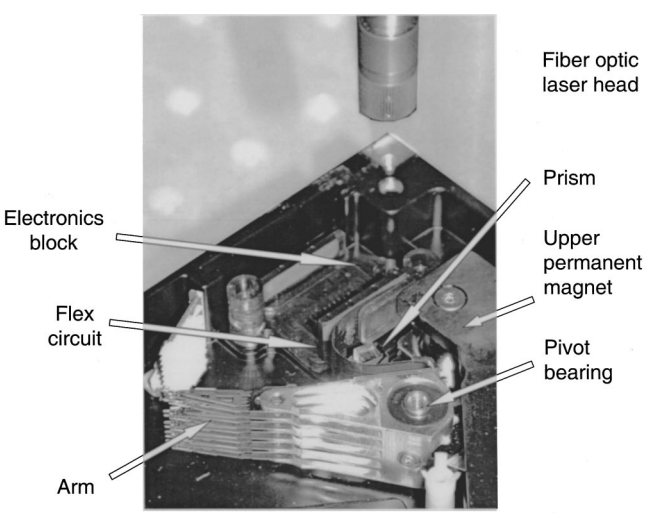

Fig. 10 Test stand used for measuring flex circuit transient responses and natural frequencies. A 90 deg prism directs the target beam from the laser head to the flex circuit. A small patch of retroreflective tape (not visible in the photograph) was placed on the circuit to reduce measurement sensitivity to misalignment and rotation of the circuit during vibration.

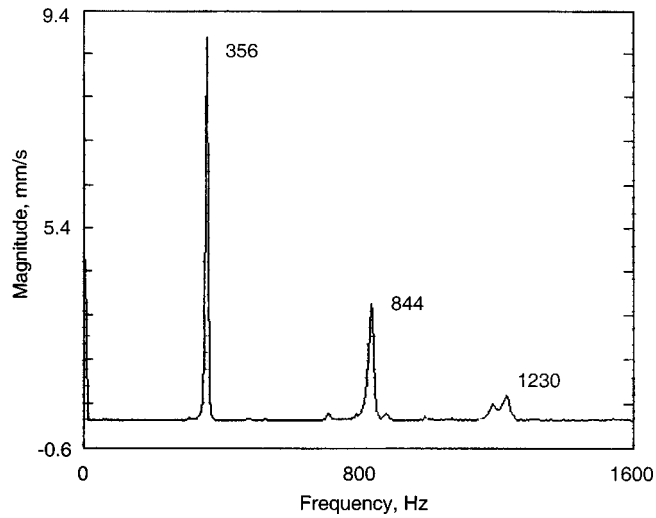

Fig. 11 Measured spectrum and natural frequencies of one disk drive's flex circuit in modes two, three, and four

$$u=\int_0^s k_* v\,ds+\overline{e}s+r\sin(\beta+\gamma)\alpha_1 \tag{19}$$

where $\overline{e}$ is the average longitudinal strain. By embedding Eq. (19) into Eqs. (11)–(13) and Eq. (15), the working form of the transverse equation of motion involves only the dependent variables v and α_1, and it is applied to characterize the lower modes.

The vibration model is discretized in terms of α_1 and nodal values for v that are evenly-spaced along the circuit's length, and the natural frequencies and mode shapes are determined numerically. Figure 9 depicts the lowest six modes on the basis of the parameters listed in Table 1. Each element of the figure is annotated to indicate the mode's natural frequency and the displacement ratio

$$\eta=\frac{R|\alpha_1|}{\max(\sqrt{u^2+v^2})}, \tag{20}$$

which measures the relative motions of the read/write head and flex circuit. At only some three Hertz, the fundamental mode is dominated by motion in α_1 and set primarily by the arm's inertia and the circuit's static stiffness. Because of its low frequency, this mode's dynamics generally do not contribute tracking errors to the extent that the modes at 374 Hz, 837 Hz, 1.39 kHz, and higher frequencies do.

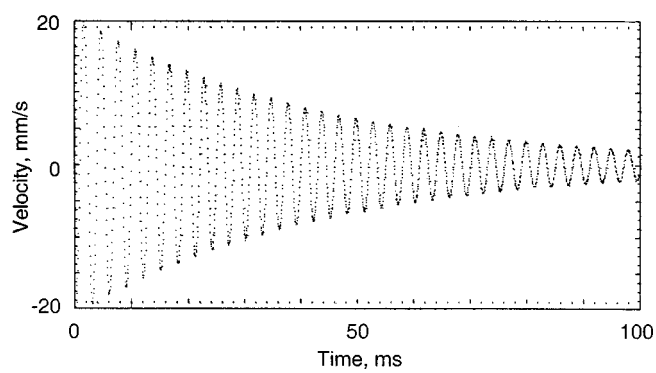

Fig. 12 Ring-down of a flex circuit in its second mode, which for this disk drive was placed at 332 Hz. The damping ratio is 1.1%.

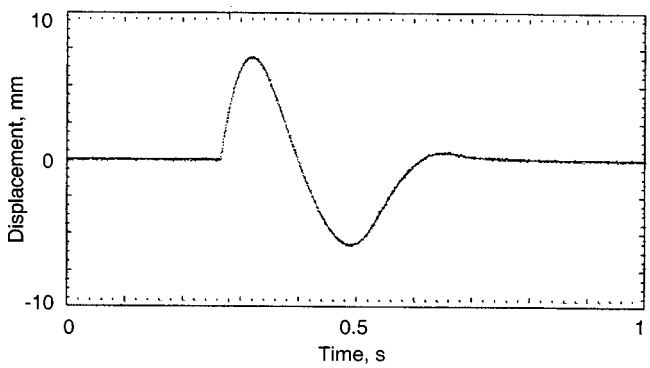

Fig. 13 Transient response in the arm and flex circuit's 3.08 Hz fundamental mode following an impact

Although the coupling ratios η are only a fraction of a percent in modes two and higher, they do have design implications because of the high precision required of this mechanism. A data track on a typical performance drive may be only 0.5 μm wide, with positioning tolerances for the heads on the track of $\pm 5\%$ (± 25 nm) for write and $\pm 10\%$ (± 50 nm) for read operations. In a situation where the flex circuit vibrates at an amplitude corresponding to one $h = 114$ μm thickness and with the coupling ratio being 0.23% in the second mode, the head would in turn respond with amplitude 260 nm, some ten times greater than the write inhibit limit.

For vibration modes that involve significant flexure of the circuit, the natural frequencies are relatively insensitive to T_* and N_*, at least for the ranges of parameters considered here. When those forces are artificially set to zero, for instance, the differences in the calculated natural frequencies for modes two through five are only 3.2%, 2.1%, 1.4%, and 0.9%, respectively. Similarly, the differences in the calculated η for those modes are only 3% or less.

Figure 10 depicts a photograph of the test stand used for measuring the flex circuit's natural frequencies. Transverse vibration was measured by using a Michelson-style laser interferometer (Polytec OFV-3000), and fiber optic leads were used to establish the paths for the reference and target light beams. The interferometer measured changes in the two light path lengths through the interference fringes generated by superposition of coherent beams that reflected from (i) a stationary reference surface and (ii) the moving flex circuit. The target beam was directed onto the flex circuit by a right-angle prism located on the concave side of the flex circuit. To ensure that sufficient light was returned by the flex circuit into the optical head, a small patch of retroreflective tape was attached to the circuit at the measurement point. Particles within the retroreflective medium ensured that a portion of the incident light was returned into the source optical fiber regardless of the flex circuit's (potentially) large displacement or slope. As the arm or circuit was impacted, the displacement or velocity signal was captured on an digital oscilloscope (HP 54600A), and its frequency content was characterized by using an dynamic signal analyzer (HP 35665A). Peaks in the autocorrelation record provided the natural frequencies. With this technique, vibration measurements were readily made with a strong signal-to-noise ratio, and with displacement resolution and bandwidth exceeding the test's requirement.

In the spectrum for one disk drive shown in Fig. 11, the natural frequencies of modes two, three, and four were measured at 356 Hz, 844 Hz, and 1.23 kHz. Several of the flex circuit's torsion modes were also present in the illustrated 1.6 kHz frequency range, but their content in Fig. 11 was suppressed by judicious placement of the impact and measurement points relative to the torsion modes' nodes. Despite its layered construction and attachments to the arm and electronics block, the flex circuit presents a damping ratio of only 1.1% in the second mode as indicated by the time record for ring-down in Fig. 12. By contrast, the mechanism is highly damped in the fundamental sway mode, with a measured frequency at 3.08 Hz. Figure 13 depicts the arm and flex circuit's transient response in that mode, and just over one cycle of motion occurred following impact.

Figures 14 and 15 show trends for the natural frequencies and coupling ratios which are predicted in a parameter study of free length L. For each length, the tension, shear force, and curvature were determined on the basis of the equilibrium configurations shown in Fig. 8. The natural frequencies for modes two through six decrease monotonically in Fig. 14 as L is examined over a range 30% below, and 30% above, the nominal value. Also for these modes, Fig. 15 depicts the behavior of the displacement ratio η. The fundamental mode is dominated by the arm's sway

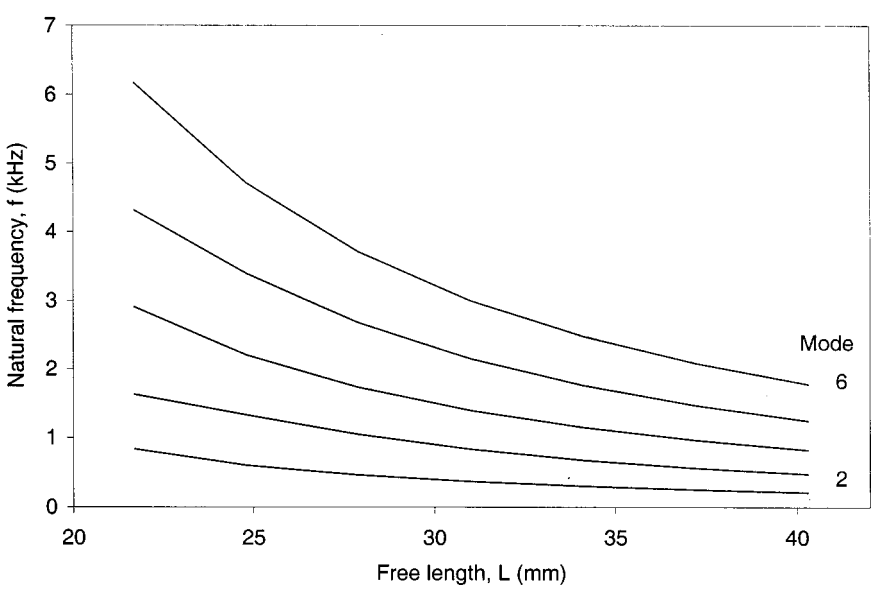

Fig. 14 Dependence of the natural frequencies in modes two through six on the flex circuit's free length

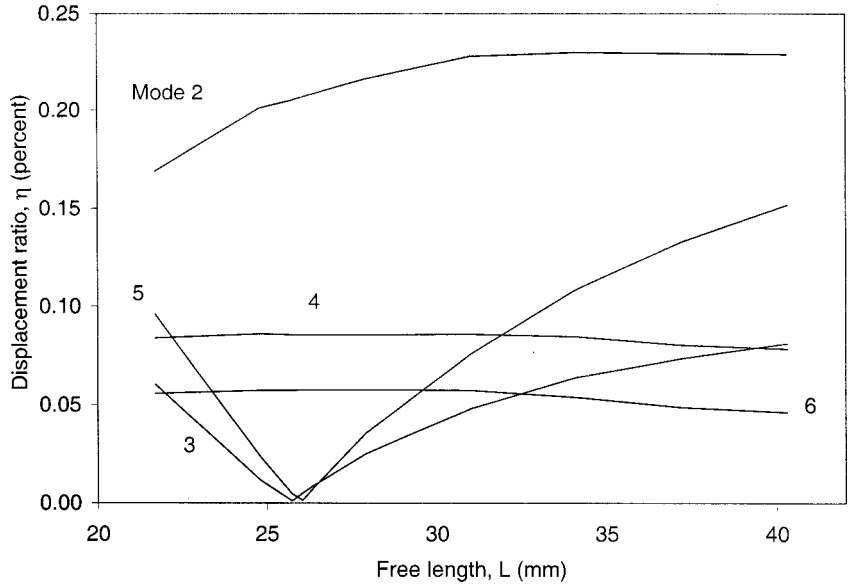

Fig. 15 Dependence of the displacement ratios η in modes two through six on the flex circuit's free length

with the flex circuit responding nearly statically, and η for that mode increases gradually within the range 357–412%. In the (even) modes two, four, and six, η is relatively insensitive to design changes in L. On the other hand, η has a zero crossing for the (odd) modes three and five at nearly the same free length ($L \approx 26$ mm) which corresponds to some 83% of the baseline value. At that design point, the natural frequencies have increased relative to their values at $L = 31$ mm in Fig. 14, and the static stiffness has likewise grown in Table 2. However, the modal displacement ratios can be reduced significantly or precisely driven to zero in modes three and five. That trade-off may be desirable in certain applications. In short, the equilibrium and vibration model can be used to advantage for optimizing flex circuit designs with respect to their vibration and load transmission performance.

5 Summary

The primary degrees of freedom for optimizing the design of flex circuits are the thickness of the layers within the circuit, its free length, and the locations and angles of the attachment points at the arm and electronics block. Those parameters can be selected with respect to three criteria: (i) the static bias torque applied by the voice coil to position the arm at a certain location on the disk; (ii) the circuit's natural frequencies relative to the control system's bandwidth; and (iii) the extent of vibration coupling between the flex circuit and the arm in certain vibration modes. The parameter study in free length is discussed with a view toward exploring the mechanism's design space and reducing arm-circuit coupling in certain vibration modes. Parameter and optimization studies with respect to the model's other degrees of freedom, and the implications of flex circuit vibration for control system design, are subjects of current investigation.

Acknowledgment

This work was supported by a grant from IBM Corporation. The author appreciates the assistance of Matthew Brake in conducting the static stiffness and natural frequency measurements. Kapton® is a registered trademark of E.I. du Pont de Nemours and Company.

References

[1] Love, A. E. H., 1944, *A Treatise on the Mathematical Theory of Elasticity*, Fourth Edition, Dover Publications, New York.
[2] Anonymous, 1996, *General Specifications*, Bulletin GS-96-7, DuPont Films, E.I. du Pont de Nemours and Company.
[3] Perkins, N. C., 1990, "Planar Vibration of an Elastica Arch: Theory and Experiment," ASME J. Vibr. Acoust., **112**, pp. 374–379.
[4] Brush, D. O., and Almroth, B. O., 1975, *Buckling of Bars, Plates, and Shells*, McGraw-Hill, New York.
[5] Wickert, J. A., 1992, "Non-linear Vibration of a Traveling Tensioned Beam," Int. J. Non-Linear Mech., **27**, pp. 503–517.